HAL
open science

Crystalline magnesium nitride (Mg3N2): From epitaxial growth to fundamental physical properties

P. John, H. Rotella, C. Deparis, G. Monge, Frédéric Georgi, P. Vennéguès, M. Leroux, J Zúñiga-Pérez

To cite this version:

P. John, H. Rotella, C. Deparis, G. Monge, Frédéric Georgi, et al.. Crystalline magnesium nitride (Mg3N2): From epitaxial growth to fundamental physical properties. Physical Review Materials, 2020, 4 (5), 10.1103/physrevmaterials.4.054601 . hal-03045516

HAL Id: hal-03045516

https://hal.science/hal-03045516v1

Submitted on 15 Dec 2020

HAL is a multi-disciplinary open access archive for the deposit and dissemination of scientific research documents, whether they are published or not. The documents may come from teaching and research institutions in France or abroad, or from public or private research centers.

L'archive ouverte pluridisciplinaire **HAL**, est destinée au dépôt et à la diffusion de documents scientifiques de niveau recherche, publiés ou non, émanant des établissements d'enseignement et de recherche français ou étrangers, des laboratoires publics ou privés.

Crystalline magnesium nitride (Mg_3N_2): from epitaxial growth to fundamental physical properties

P. John[1], H. Rotella[1], C. Deparis[1], G. Monge[2], F. Georgi[2], P. Vennéguès[1], M. Leroux[1], and J. Zuniga-Perez[1,*]

[1] CRHEA, CNRS, UCA, Rue Bernard Gregory, 06560 Valbonne, France
[2] CEMEF-MINES ParisTech, 1 rue Claude Dannesse, 06904 Sophia Antipolis Cedex, France

*Corresponding author: jzp@crhea.cnrs.fr

Abstract

Single-crystalline Mg_3N_2 thin films are grown on MgO(100) substrates by plasma-assisted molecular beam epitaxy. To prevent the oxidation of the Mg_3N_2 films and allow further physical characterization, a polycrystalline MgO cap is deposited in-situ. The growth orientation of the Mg_3N_2 films can be tuned from (100) to (111) by changing the growth conditions and the associated epitaxial relationships have been determined by means of X-ray diffraction. The lattice constant of Mg_3N_2 films has been monitored as a function of temperature from 300 K to 900 K, determining thereby the linear thermal expansion coefficient. Transmission measurements indicate an optical bandgap of crystalline Mg_3N_2 around 2.9 eV at room-temperature, consistent with diffuse reflectance measurements on micrometric Mg_3N_2 particles. These results demonstrate the possibility of exploiting Mg_3N_2 as a new crystalline semiconductor in the blue-violet range.

I. INTRODUCTION

The study of new semiconductors requires the synthesis of high-quality material to ensure that the measurement of fundamental physical properties such as lattice parameters, electron effective mass or bandgap is not perturbed by the presence of defects. A prototypical example is InN, whose bandgap was considered for many years to be about 1.9 eV (see [1] and references therein). Once samples of high-enough quality became available in the early 2000s [2,3], its actual bandgap could be reliably measured to be about 0.7 eV.

Another nitride, Mg_3N_2, lives today a similar situation. This is rather surprising given that its anti-bixbyite structure and its lattice parameters were measured on powder samples and mm-long single crystals as soon as 1933 [4], being later refined in the nineties [5]. Ceramic Mg_3N_2 has been used in industry for years as a nitriding agent for the formation of various nitrides [6, 7], and as a catalyst for the synthesis of superhard silicon nitride and cubic boron nitride [8]. More recently, it has found its own applications as high-thermal conductivity ceramics when doped with silicon [9] and as a reversible hydrogen storage material [10]. Interestingly, all these applications use magnesium nitride for its physicochemical properties while none exploits its optoelectronic ones.

The few theoretical calculations that exist on crystalline Mg_3N_2 predict it to be a semiconductor with an energy gap between 1.1 eV to 2.26 eV, depending on the actual calculation method [11,12,13]. Two of these works [11,12] indicate a direct bandgap, while the third calculation [13] finds an energy difference of about 10 meV between the indirect and direct transitions that would result, in practice, in a direct character semiconductor. However, these values are far from those evaluated experimentally, which range from a minimum measured value of 2.5 eV obtained by transmission measurements [14], through 2.8 eV-2.9 eV as determined by reflectance and photoluminescence excitations measurements [11, 15], respectively, to a largest value of 3.15 eV at room-temperature measured by reflectance measurements too [16]. Besides the basic interest on the fundamental properties of a new material, determining its electronic properties can also be relevant from a

technological point of view. In the case of Mg_3N_2 this applicative interest arises in the context of solar energy, since by alloying it with Zn_3N_2 one can tune its absorption edge to an optimum of 1.4 eV [17], and especially in the context of GaN-based optoelectronics. Indeed, Mg_3N_2 has been detected in highly-doped GaN:Mg samples [18,19,20] and has been shown to decrease the *p*-doping level. Given the widespread use of GaN optoelectronic devices, including light-emitting diodes and laser diodes, and the usage of Mg as its only efficient *p*-dopant, unravelling the basic electronic properties of Mg_3N_2 is of major technological relevance.

In this article we discuss the epitaxial growth of Mg_3N_2 thin films by molecular beam epitaxy (MBE) and we analyze their structural properties by X-ray reflectivity (XRR) and high-resolution X-ray diffraction (HRXRD), paying special attention in demonstrating their epitaxial character. Before studying the films physical properties, the *in-situ* deposition of a protective MgO layer will be examined as a means of preventing the otherwise irreversible decomposition of the Mg_3N_2 films when exposed to air. Subsequently, the structural quality of the films and the evolution of lattice parameter with temperature will be evaluated. Finally, the optical bandgap of such epitaxial films will be measured and compared to that of commercially-available Mg_3N_2 microparticles.

II. EXPERIMENTAL METHODS

Epitaxial Mg_3N_2 thin films, with thicknesses typically in the 100 nm range, were grown by plasma-assisted MBE on commercial MgO(100) substrates purchased from CRYSTAL. The substrates were prepared by rapid thermal annealing for 2 minutes at 1150 °C under oxygen atmosphere in order to achieve an atomically-flat step-and-terrace morphology. Growth was then performed in a Riber EPINEAT II-VI system equipped with an effusion cell for elemental Mg (6N). High purity nitrogen and oxygen gases (6N) were introduced through radio-frequency plasma cells operated at a power of 360 W and 400 W, respectively. The substrate temperature was measured with a pyrometer directed

onto the sample. *In-situ* optical reflectivity and reflection high-energy electron diffraction (RHEED) were used to monitor the growth rate and characterize the surface crystallinity.

The surface morphology of the MgO capping films was measured by atomic force microscopy (AFM) using a Bruker Edge system, while the structural properties of the Mg_3N_2 films were evaluated by HRXRD and XRR using a Panalytical X'Pert Pro MRD system using Cu $K_{\alpha 1}$ radiation. The temperature-dependent XRD measurements were performed in an Empyrean Panalytical using both Cu $K_{\alpha 1}$ and $K_{\alpha 2}$ lines and a polycapillary as incident optics. The samples were kept in a closed chamber (Anton Paar) and nitrogen was flown through continuously during the measurements and the temperature ramps. X-ray photoelectron spectroscopy (XPS) has been used to qualify the films composition. The measurements have been carried out in a Thermo Scientific system equipped with an Al K_{α} monochromated source, a low energy flood-gun for charge compensation and an Ar^+ ion gun for depth profiling. Finally, white-light transmission and reflectance measurements were employed to measure the absorption coefficient and diffuse scattering, respectively.

III. REACTIVITY OF Mg_3N_2 UPON AIR EXPOSURE: MgO CAPPING LAYER

Mg_3N_2 is known to decompose under ambient conditions, reacting in particular with water. This process leads to the formation of oxides, oxynitrides and, mostly, magnesium hydroxides [21,22,23]. To quantify the speed at which decomposition occurs we purchased commercial Mg_3N_2 powder from Alfa Aesar (99.5 % purity) with a nominal particle size of 44 μm, which was confirmed by scanning electron microscopy measurements revealing particle sizes in the same scale.

Figure 1 presents the XRD patterns of the Mg_3N_2 powder kept under ambient conditions as a function of time. Initially the powder is yellowish in colour, while after reaction in air it becomes completely white and increases drastically in volume. It appears after one hour of exposure to air that the powder begins to decompose. Although no XRD signal from $Mg(OH)_2$ is yet visible, the intensity of the Mg_3N_2 peaks decreases already. Indeed, initially only the surface of the micrometric particles is decomposed, and only when the reaction spreads into the volume a signal is detected from the magnesium

hydroxide phase, which ends up dominating the XRD pattern after 24 hours. To assess quantitatively the decomposition kinetics of the Mg_3N_2 powder we evaluated the peak areas of the four reflections shown in Figure 1 as a function of time. Using an exponential fit for the peak areas we obtain a mean time constant, averaged over all four reflections, of $\tau_{decompostion}$ = 5.5±0.2 h in ambient conditions.

Since the thin films grown in this study, with thicknesses in the 100 nm range, display a larger surface-to-volume ratio than the microparticles discussed above (44 μm in diameter), their decomposition rate can be expected to be even larger than that of the powder. Thus, it is absolutely necessary to develop a capping layer that can be deposited in the MBE reactor prior to the removal of the Mg_3N_2 films and their exposure to air.

Due to its high chemical stability and ionic Mg-O bond nature (cohesive energy of 10.33 eV [24]), MgO seems a suitable candidate, though counterintuitive due to the presence of oxygen in the compound. If we assume, as will be confirmed in the following, that the oxygen from the MgO cap does not react with the underlying Mg_3N_2, one still needs to insure that the quality of the capping, in particular its compactness, is sufficient to prevent contact between the film and the ambient moisture. Thus, the optimization parameter for the MgO cap has been chosen to be the surface roughness. MgO thin films were grown homoepitaxially in the same MBE reactor on MgO(100) substrates. Prior to growth, the substrates were annealed *ex-situ* at high temperature (~1150 °C) so as to remove any polishing residue/scratch from their surface and promote the formation of atomically-flat terraces, as illustrated by the AFM image (see Figure 2). A complete series of samples was analyzed by AFM: Figure 2 displays the roughness evolution as a function of growth temperature and oxygen flow, the z scale providing the root mean square roughness extracted from the analysis of 2×2 μm^2 images.

At low substrate temperature and oxygen flow, Figure 2(a), the surface exhibits cubic grains with a height and width of about 100 nm but displays an incomplete wetting of the substrate, which is unacceptable for the current use. An increase of oxygen flow at intermediate temperatures slows down (eventually prevents) MgO growth, with nucleation taking place randomly on the substrate and leading to isolated agglomerates (Figure 2(b)). At the highest substrate temperature (~650 °C) and

large oxygen flow (0.40 sccm, Figure 2(c)), nucleation occurs along the atomic steps present on the annealed substrate. The MgO crystallites have a cubic shape with a 40 nm base. Finally, at temperatures around 580 °C and oxygen flows around 0.35 sccm, Figure 2(d), the substrate surface is completely wetted and the roughness (1.4 nm) is the lowest of the series. For these optimized conditions, the MgO film consists of square grains with lateral sizes of 40 nm and heights, above the mean surface, between 1 and 5 nm. Under these growth conditions an MgO growth rate of 63 nm/h has been measured by XRR on a MgO/CdO multilayer structure. In the following, all the Mg_3N_2 films were covered with a nominally 50 nm thick MgO cap grown under the optimized conditions.

IV. Mg_3N_2 EPITAXIAL GROWTH: CRYSTAL ORIENTATION TUNABILITY

Figure 3 illustrates the effect of Mg/N ratio and temperature on the growth orientation of ~100 nm thick Mg_3N_2 thin films grown on MgO(100) substrates. Note that the XRD patterns were recorded with a fully opened detector to detect any possible contribution from parasitic phases. At 400 °C and the smallest Mg/N ratio the growth direction is unique and parallel to [100], consistent with a recent study reporting first attempts to grow single-crystal Mg_3N_2 films [14]. Note that a shoulder on the lower side of the MgO substrate (200) peak, which might be attributed to MgON formed at the substrate/layer interface, appears under these growth conditions. Furthermore, the associated RHEED pattern (Inset (A) in Figure 3(a)) is streaky for the first ~20 nm, but becomes spotty afterwards, the spots being elongated along circular arcs as the growth proceeds. Under these growth conditions, the thicker the thin film the worse the structural quality, as attested by the increase of the circular arcs length (indicating an increase of the relative twist of the grains). The in-plane lattice parameter of Mg_3N_2 (200) was determined from the RHEED pattern to be 4.65±0.24 Å, indicating a strong compressive in-plane strain with respect to the relaxed lattice (literature value of 4.976 Å) at the beginning of the growth. As the nitrogen flow is diminished, the (100) orientation is maintained while the parasitic MgON phase disappears completely. A further reduction of the nitrogen flow leads to the appearance of grains oriented parallel to [111], giving rise to polycrystalline thin films displaying concomitantly (111) and

(100) grains. Interestingly, a further reduction of the nitrogen flow and/or increase of the Mg cell temperature (i.e. an increase of the Mg/N ratio) results in Mg_3N_2 thin films displaying again one single orientation, but this time (111). The RHEED pattern, which is still spotty (Inset (E) in Figure 3(a)), can be modeled with diffraction from three families of crystallographic planes, as represented by the coloured dots in Inset (E). The exact epitaxial relationships giving rise to such a diffraction pattern will be discussed in Section V. If under these last growth conditions we increase the growth temperature, we recover a streaky RHEED pattern corresponding to a flat (111) surface (Inset (F) in Figure 3(a)). It is thus possible to tune the growth orientation of Mg_3N_2 on MgO(100) from (100) to (111) by switching from N-rich to more Mg-rich growth conditions.

As shown in Figure 3(b), where the growth rate of Mg_3N_2 films is plotted as a function of the Mg cell temperature for a nitrogen flow of 0.35 sccm, the increase of Mg flux results also in an acceleration of the growth rate. This is an important aspect to keep in mind given that, similarly to other nitrides grown by plasma-assisted MBE (e.g. GaN or AlN), the actual growth rates are rather low (typically in the order of 2 nm/min for optimized growth conditions). Indeed, the maximum growth rates we have achieved are in the order of 2.6 nm/min (equivalently, 312 nm/h), not shown here, but this requires either low temperatures and/or large N flow and Mg flux, far from the optimum growth conditions to achieve high-quality thin films. The increase of the growth rate up to a Mg cell temperature of 420 °C to 430 °C (see Figure 2(b)) indicates a growth regime limited by Mg incorporation (i.e. N-rich). On the other hand, the saturation of the growth rate at a Mg cell temperature larger than 420 °C to 430 °C indicates an excess of Mg, i.e. Mg-rich conditions. The detailed growth conditions of samples A to G are displayed in Table I.

Before demonstrating the epitaxial character of the grown films and assessing some of their physical properties, let us discuss the role of the MgO cap. XPS measurements (not shown) enable to monitor the 1:1 (Mg:O) stoichiometry of the MgO cap as well as the presence of the underlying Mg_3N_2 thin film, which is measured thanks to *in-situ* etching. However, the presence of oxygen in the capping layer prevents any quantitative analysis of the Mg_3N_2 stoichiometry. The reason is that this cap must be

eroded *in-situ* in the XPS chamber and, thus, a non-negligible background oxygen partial pressure is always present in the chamber when analyzing the underlying Mg_3N_2 film and can oxidize it. This effect can be readily monitored in time, the oxygen concentration detected when eroding the Mg_3N_2 slowly increasing as a function of the time passed between the erosion of the MgO and the measurement. To assess the abruptness of the MgO(cap)/Mg_3N_2(film) interface we have systematically employed XRR. Figure 4 shows a typical X-ray reflectivity curve, measured on sample F from the series discussed above, displaying neat interference fringes. The fitting of the curve using the GenX software [25] indicates a total MgO cap thickness of 42 nm and a total Mg_3N_2 thickness of 98 nm. Most importantly, there is no indication of any interfacial layer between the two films and the Mg_3N_2 roughness is in the order of 1 nm, consistent with the observation of a streaky RHEED pattern measured at the end of the Mg_3N_2 growth. In contrast, a roughness of 2.2 nm was extracted from the XRR of sample E (not shown here), being consistent with the observation of a spotty RHEED pattern. Note that the damping of the interference fringes at large 2θ angles for sample F in Figure 4 (displaying a streaky pattern) is caused by the MgO capping layer that displays a roughness of 5 nm. Note also that the Mg_3N_2 density extracted from the fitting, 2.56 g cm^{-3}, is about 5 % smaller than the tabulated density of Mg_3N_2. While such discrepancies are often encountered in XRR measurements, they might also indicate a large vacancy density or the existence of grain boundaries.

V. Mg_3N_2 EPITAXIAL GROWTH: STRUCTURAL QUALITY AND EPITAXIAL RELATIONSHIPS

As highlighted in the introduction, our main objective was to develop high-quality Mg_3N_2 films to be able to assess their physical properties. One previous attempt in 2018 to grow such films by MBE (reference [14]) indicated that for films thinner than 800 nm the diffraction intensity was "barely detectable". According to the authors of this study, the reason was the presence of only light elements (Mg and N) in the film, leading to an overall diffracted intensity five orders of magnitude smaller than that of the MgO substrate (which, incidentally, consists also of light elements).

Figure 5(a) shows the XRD 2θ/ω scan of sample F using a 1/4° slit in the diffraction path. Besides confirming that no parasitic phases or orientations apart from the (111) are detected, it is noteworthy that a 100 nm thick Mg_3N_2 film results in a diffracted intensity that is "just" three to four orders of magnitude smaller in intensity than that of the MgO(100) substrate, and well above the background level. This clearly indicates that Mg_3N_2 films, even thin ones, can provide strong X-ray diffraction, as soon as their crystalline quality is sufficiently high. To further illustrate the quality of the current Mg_3N_2 films and compare them with other standard semiconductors, Figure 5(b) shows the 2θ/ω scan around the Mg_3N_2 (222) reflection from the same sample recorded with a crystal analyzer (i.e. in triple axis configuration). The additional intensity peaks surrounding the main one arise due to finite-size effects along the growth direction and indicate a large degree of coherence along the longitudinal direction. This finite-size effect can be used to estimate very precisely the average film thickness. To do so we have simulated the X-ray diffraction pattern (red curve in Figure 5(b)) considering a perfect crystal along the growth direction (i.e. perfect X-ray coherence) and no surface roughness. Under these assumptions the diffractogram is given by [26]

$$I(\theta) = L(\theta) + F_{hkl}^2 \cdot \frac{sin^2(2\pi n_{hkl}\sin(\theta/\lambda))}{sin^2(2\pi d_{hkl}\sin(\theta/\lambda))} \quad (1)$$

where $L(\theta)$ is a Lorentzian function representing the diffuse scattering term, F_{hkl} is the structure factor associated to the (*hkl*) reflection, *n* the number of unit cells along the [*hkl*] direction, d_{hkl} the interreticular distance between (*hkl*) planes, and λ the employed X-ray wavelength (1.54056 Å, in our case). The best fit to our pattern gives an average out-of-plane lattice parameter of 2.869±0.001 Å (literature value for fully-relaxed: 2.873 Å) and a total thickness of 339±1 unit cells. The corresponding thickness is 97.3 nm, which perfectly matches the thickness determined by XRR presented in the previous section. Note that our simulation does not reproduce the asymmetry between the low-angle and high-angle sides of the (222) peak, given that we have considered a homogenous strain state along the growth direction. This asymmetry reveals in fact the existence of an in-plane strain (and/or compositional) gradient that relaxes along the growth direction [26,27], the Mg_3N_2 films being under more compressive in-plane strain closer to the substrate. This is consistent with the slight

misalignment between the simulated RHEED patterns (calculated with fully-relaxed lattice parameters) and the experimental ones, shown in Inset (E) of Figure 3(a). The measured spacings between reciprocal lattice points indicate an in-plane (220) interplanar distance of 3.46±0.31 Å (literature: 3.519 Å) and an out-of-plane (222) interplanar distance of 2.94±0.37 Å (literature: 2.873 Å). Thus, both XRD 2θ/ω scans an RHEED patterns confirm the in-plane compressive strain close to the film/substrate interface.

To assess the epitaxial character of the current films their in-plane orientation with respect to the MgO(100) substrate has been determined by measuring ϕ-scans on asymmetrical reflections, the azimuth ϕ being defined as the angle by which the sample is rotated around an axis perpendicular to its surface. The results are presented in Figure 6. In principle, the out-of-plane crystallographic direction being [111], only three peaks are expected in the ϕ-scan for the set of {440} planes. Instead, we find experimentally twelve peaks (Figure 6(a)). In order to account for this fact we must restore to the theory of epitaxial domains formation developed by Grundmann *et al*. [28,29]: it indicates that due to the rotational mismatch between the three-fold symmetric film and the four-fold symmetric substrate (Figure 6(b)), four crystalline epitaxial domains are to be expected, leading to twelve peaks in the XRD ϕ-scan. The in-plane orientations of the four epitaxial domains are schematically represented in Figure 6(c). Thus, the epitaxial relationships of our Mg_3N_2(111)/MgO(100) films are given by

$$[1\bar{1}0]Mg_3N_2 \| [011]MgO$$

$$[11\bar{2}]Mg_3N_2 \| [01\bar{1}]MgO$$

plus the three additional rotational domains obtained by rotating the Mg_3N_2 structure by 90°, 180° and 270° around the Mg_3N_2[111] direction normal to the surface. This result is in agreement with the RHEED pattern given in Inset (E) of Figure 3(a). Its simulation was performed using the epitaxial relations given above and the colours of the points correspond to the different epitaxial domains illustrated in Figure 6(c): The red dots represent the simulated diffraction pattern of $\{1\bar{1}0\}$ planes of the domain indicated in red, the yellow dots arise from the $\{1\bar{1}0\}$ planes of the domain indicated in

yellow and the blue dots correspond to the diffraction of $\{11\bar{2}\}$ planes of the domains indicated in blue and black in Figure 6(c).

The knowledge of the epitaxial relationships allows us also to develop an atomic model of the Mg_3N_2(111)/MgO(100) interface, as displayed in Figure 6(d). In this atomic configuration the lattice mismatches between Mg_3N_2 and MgO (2.3 % along Mg_3N_2 $[11\bar{2}]$ and 18.2 % along Mg_3N_2 $[1\bar{1}0]$, calculated with a domain phase matching condition of two MgO unit cells for one Mg_3N_2 cell) do indicate a strong compressive strain on the Mg_3N_2 films, consistent with the asymmetry discussed in Figure 5(b). Note finally that, as suggested by the above-mentioned theory, if rotational domains were to be eliminated while keeping the same crystal orientation, a means of rotational symmetry-breaking should be employed, e.g. by using voluntarily misoriented (100) substrates. Alternatively, other substrate orientations (e.g. MgO(111)) could be used.

VI. LINEAR THERMAL EXPANSION COEFFICIENTS OF EPITAXIAL Mg_3N_2

Since for most materials epitaxy is carried out at temperatures greater than room temperature, the knowledge of their linear thermal expansion coefficient is essential in order to quantitatively analyze the lattice mismatch between thin film and substrate at the actual growth temperature. This, in turn, can enable the design of heterostructures sustaining pseudomorphic growth or, on the contrary, maximizing the initial strain of the film in order to favor rapid plastic relaxation. Besides, the thermal expansion coefficient influences numerous basic physical properties whenever temperature variations come into play; in particular, it can play an essential role in determining the temperature-dependence of the material bandgap [30].

To assess the linear thermal expansion coefficient α_T [31] of the Mg_3N_2 epitaxial films, as well as of the MgO substrate, we have measured the out-of-plane lattice parameters (see Figure 7(a) for the Mg_3N_2 thin films) as a function of temperature in the temperature range from 300 K up to 1100 K. In order to minimize systematic errors, we have employed the methodology introduced by Liu and Zheng to measure precisely the thermal expansion coefficient of silicon [32,33]. Figure 7(b) shows the variation

of the Mg_3N_2 (111) and MgO(100) interplanar distances as a function of temperature. For temperatures above 900 K no data points for Mg_3N_2 are given, as its diffraction intensity decreases enormously. This points towards a pure thermal stability issue, given that all measurements were carried out under nitrogen atmosphere and no sign of oxidation could be detected in the XRD patterns. From the interplanar distances curves the expansion of both Mg_3N_2 and MgO is seen to be linear in the current temperature range. The averaged linear thermal expansion coefficients obtained from a linear fit to all available data are $1.14\pm0.03\times10^{-5}$ K^{-1} and $1.30\pm0.02\times10^{-5}$ K^{-1} for Mg_3N_2 and MgO, respectively, and their applicability range corresponds to 300-900 K and 300-1100 K, respectively. As displayed in Figures 8(a) and (b), a linear thermal expansion coefficient has been extracted point by point using

$$\alpha_T = \frac{d_{perp}(T+\Delta T)-d_{perp}(T)}{\frac{1}{2}\cdot(d_{perp}(T+\Delta T)+d_{perp}(T))\cdot\Delta T} \quad (2)$$

where d_{perp} corresponds to the out-of-plane lattice parameter, T is the temperature and ΔT corresponds to the temperature difference between consecutive points.

The thermal expansion of MgO has been thoroughly studied previously given its common use as refractory material (see 34 and 35, and references therein). Our determination is consistent with the linear thermal expansion coefficients published in the 300-1200 K range (Figure 8(a)), which fall within the $1.05\text{-}1.53\times10^{-5}$ K^{-1} window. On the other hand, to our knowledge there is just one previous report on the thermal expansion coefficient of Mg_3N_2 powder [36], which was conducted only in the low-temperature range (from 10 K to 300 K). Our data are thus complementary, as they extend the knowledge of the Mg_3N_2 thermal expansion coefficient to higher temperatures. By combining both sets of data (Figure 8(b)) we can reproduce the well-known behavior of the thermal expansion coefficient as a function of temperature of numerous semiconductors. This prototypical form, with a fast increase of the thermal expansion coefficient at low temperatures and its saturation at high enough temperatures, can be explained by the selective excitation of acoustic and optical phonons [37,38,39]. Finally, it should be noted that our measurements indicate that Mg_3N_2 has a thermal expansion coefficient that is comparable to that of cubic BN [40], and roughly two to three times larger than that of AlN [39] and GaN [41].

VII. BANDGAP OF EPITAXIAL Mg_3N_2

To measure the optical bandgap of epitaxial Mg_3N_2 films and determine its temperature dependence, transmission measurements were carried out from low (~10 K) to room-temperature and the absorption coefficient (α) was extracted therefrom. Besides, to be able to compare with previous measurements carried out on Mg_3N_2 powder samples, we also measured diffuse reflectance as a function of temperature on the same micrometric Mg_3N_2 particles that we have employed in Section III to analyze the chemical reactivity of Mg_3N_2 in ambient conditions.

As shown in Figures 9(a) and 9(b), where we have plotted the square of αE as a function of the photon energy E for our thin films, a bandgap of about 2.95 eV can be estimated at low temperature, which shrinks down to 2.88 eV when increasing temperature to 300 K. These measurements give values consistent with some of the previous measurements on Mg_3N_2 powder samples [11,15], represented by dots in Figure 9(c), as well as with our own measurements on commercial Mg_3N_2 microparticles (triangles in Figure 9(c)). As for many other semiconductors, the measured temperature dependence of the bandgap can be fitted by the so-called Varshni formula [42]:

$$E_g(T) = E_0 - \delta T^2/(T + \beta) \tag{3}$$

where T is the temperature, E_0 is the bandgap energy at 0 K and δ and β are constants to be extracted from the fit. Similarly, the temperature dependence of the energy bandgap can be also described by the more physically-meaningful model developed by K. O'Donnell *et al*. [43], which considers electron-phonon coupling and takes into account the phonon density of states and their Bose-Einstein occupation probability:

$$E_g(T) = E_0 - 2\alpha_B\Theta_B\left[coth\left(\frac{\Theta_B}{2T}\right) - 1\right] \tag{4}$$

with α_B and $k\Theta_B$ being the coupling constant and the average phonon energy, respectively. Table II gives the values for the three parameters defining each of the models for a typical Mg_3N_2 film as well as for the commercial Mg_3N_2 powder.

Note first that the bandgap value at room temperature measured on our thin films as well as on the powder (both, ours and that used in reference [15]) coincide, indicating a Mg_3N_2 bandgap at room-temperature of about 2.90 eV. It is however surprising that the bandgap shrinkage between room-temperature and 10 K is different: while the 70-100 meV bandgap shrinkage in our thin films is comparable to that observed in standard semiconductors such as GaAs or GaN [44], the bandgap shrinkage measured on the Mg_3N_2 powder is relatively large (~150 meV) compared to other semiconductors.

Indeed, if we assume that the absorption band edge we measure corresponds to transitions between the same two bands in the whole temperature range (note that band crossings cannot be totally excluded considering the theoretical calculations discussed in Section I), then its shift with temperature depends only on two terms. The first one is associated to the thermal expansion of the lattice and the second one is linked to the band energies renormalization due to electron-phonon interactions [30]. While in most cases the second term dominates [45], one might hypothesize that the relatively large thermal expansion coefficient of Mg_3N_2 might result for the current material in a non-negligible contribution of the thermal expansion to the shrinkage of the bandgap. However, if this were the sole reason explaining the strong bandgap shrinkage then we would have expected an even larger shrinkage for our Mg_3N_2 thin films, which are epitaxially "attached" to a substrate with a slightly larger thermal expansion coefficient.

Overall, while the precise temperature evolution of the Mg_3N_2 bandgap and, in general, the electronic band structure of Mg_3N_2 requires further work, our study allows discriminating between previous measurements and enables to establish the Mg_3N_2 bandgap to be in the blue-violet wavelength range.

VIII. CONCLUSION

Mg_3N_2 thin films have been grown along the [111] direction on MgO(100) substrates and their epitaxial character assessed. Thanks to these high-quality films the linear thermal expansion coefficient of the material has been measured for the first time for temperatures above room-temperature

(α_T ~1.20×10^{-5} K^{-1}), and its optical bandgap has been determined to be about 2.95 eV at low temperature and confronted to that of Mg_3N_2 microparticles. Overall, this work paves the way to exploit a new nitride material in wide bandgap optoelectronic applications and adds to other nitrides recently introduced (e.g. AlSiN [46,47]).

Acknowledgments

We acknowledge support from ANR through the project ZONE (ANR-17-CE24-0043-01).

Figures Caption

Figure 1: $2\theta/\omega$ scans recorded at ambient conditions on commercial Mg_3N_2 microparticles from Alfa Aesar (99.5 %) as a function of time. For air exposures shorter than 6 h, peaks corresponding to diffraction from (222), (213), (004) and (233) Mg_3N_2 planes are observed, while for longer exposures only a broad peak corresponding to $Mg(OH)_2$ is recorded. Insets show photographs of (a) the initial powder and (b) the powder after 24 h.

Figure 2: MgO(100) homoepitaxy. RMS roughness extracted from 2x2 μm^2 AFM images as a function of growth temperature and O_2 flow. The inset shows the AFM image of an MgO(100) substrate after high-temperature annealing. (a)-(d) AFM images corresponding to the samples referenced by capital letters on the growth parameters diagram. The images size is the same and the scale is indicated in (d). The Z-scale in the four images corresponds to the maximum height.

Figure 3: (a) $2\theta/\omega$ scans on Mg_3N_2 thin films grown on MgO(100) substrates and capped by a 50 nm-thick MgO layer. The letters A to F refer to the different growth conditions reported in Table I. RHEED patterns of selected samples, where (S) corresponds to the MgO substrate prior to the Mg_3N_2 growth and (A), (E) and (F) correspond to the samples A, E and F, respectively. (b) Growth rate of Mg_3N_2 thin films as a function of Mg cell temperature for a constant N_2 flow of 0.35 sccm. The detailed growth conditions for sample G are reported in Table I as well.

Figure 4: XRR curve measured on sample F. The fit of the XRR curve has been performed using the GenX software.

Figure 5: (a) Large range $2\theta/\omega$ scan on a Mg_3N_2 thin film (sample F) measured with a 1/4° slit. (b) $2\theta/\omega$ scan around the Mg_3N_2 (222) reflection from the same sample in (a) performed with a crystal analyzer. The fit in (b) uses Equation (1).

Figure 6: XRD ϕ-scans on (a) Mg_3N_2 {440} planes and (b) MgO {220} planes. (c) Schematic representation of the four Mg_3N_2 rotational domains. (d) Schematic atomic model displaying the epitaxial relationship of one of the Mg_3N_2 domains. The large dots correspond to the Mg atoms of the MgO substrate while the small dots correspond to the N atoms of the Mg_3N_2 thin film. O atoms of the MgO substrate and Mg atoms of the Mg_3N_2 layer were omitted for clarity. This leads for the MgO substrate to a square atomic lattice, given that Mg atoms from two consecutive (100) planes are represented.

Figure 7: (a) $2\theta/\omega$ scans around the Mg_3N_2 (222) reflection for different temperatures, illustrating the temperature-dependent lattice expansion. The dashed line is just a guide for the eyes. (b) Out-of-plane interplanar distances for the Mg_3N_2 film and the MgO substrate as a function of temperature.

Figure 8: (a) Linear thermal expansion coefficient point by point for the MgO substrate, compared to previous published values (reference [35]). (b) Linear thermal expansion coefficient point by point for the Mg_3N_2 film and previously published values at low temperatures (reference [36]). The linear thermal expansion coefficients have been calculated from Equation (2). Note that the horizontal (temperature) scales are not the same for (a) and (b).

Figure 9: Plot of $(aE)^2$ as a function of photon energy for Mg_3N_2 thin films at (a) 12 K and (b) 300 K. (c) Temperature dependence of the optical bandgap of Mg_3N_2 thin films measured by transmission

(squares), of Mg_3N_2 powder measured by diffuse reflectance in this work (triangles), as well as previous values extracted from PLE spectra in reference [15]. The dashed lines in figure (c) correspond to the fit of the experimental data to O'Donnell's model (reference [43]).

Tables Caption

Table I: Growth conditions of the series of Mg_3N_2 thin films grown on MgO(100) substrates and capped with an MgO layer.

Table II: Fitting parameters of the Varshni phenomenological formula (first three rows) and O'Donnell's model (second three rows) for the temperature dependence of the bandgap. The fitting parameters have been determined for a typical Mg_3N_2 epitaxial thin film and the commercial Mg_3N_2 powder.

Table I:

Sample	Growth temperature (°C)	Mg cell temperature (°C)	Nitrogen flow (sccm)	Thickness (nm)	Orientation
A	400	410	1	168	(100)+MgON
B	400	410	0.5	110	(100)
C	400	410	0.35	73	(100)+(111)
D	400	420	0.35	92	(100)+(111)
E	400	430	0.35	98	(111)
F	460	430	0.35	97	(111)
G	400	440	0.35	94	(111)

Table II:

	Thin film	Powder
E_0(eV)	2.93	3.06
δ(eV/K)	$4.01 \cdot 10^{-3}$	$4.03 \cdot 10^{-3}$
β(K)	5187	1882
E_0(eV)	2.94	3.05
α_B(eV/K)	$8.91 \cdot 10^{-5}$	$2.92 \cdot 10^{-4}$
$k\theta_B$(meV)	23	35

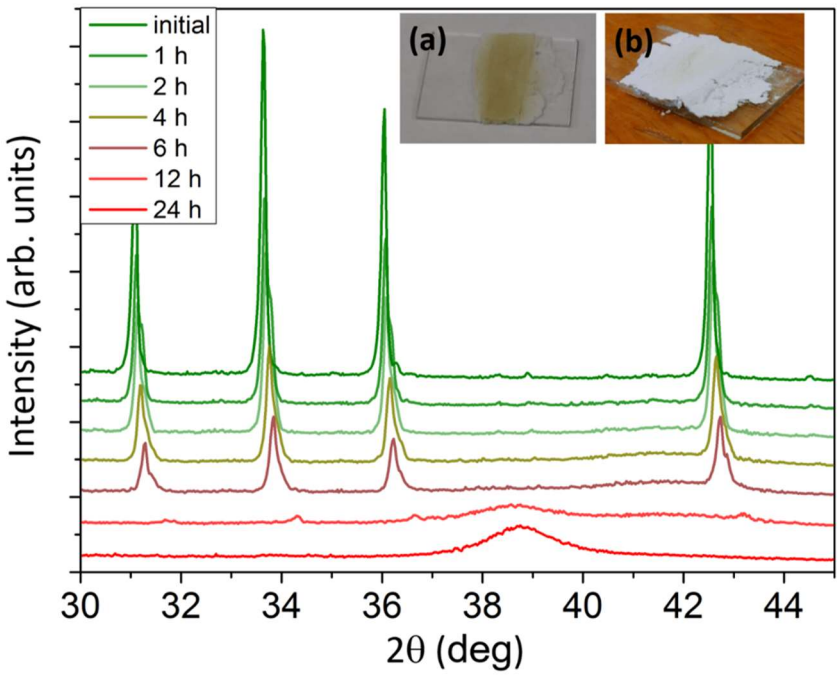
initial
1 h
2 h
4 h
6 h
12 h
24 h
(a)
(b)
Intensity (arb. units)
30
32
34
36
38
40
42
44
2θ (deg)

Figure 1

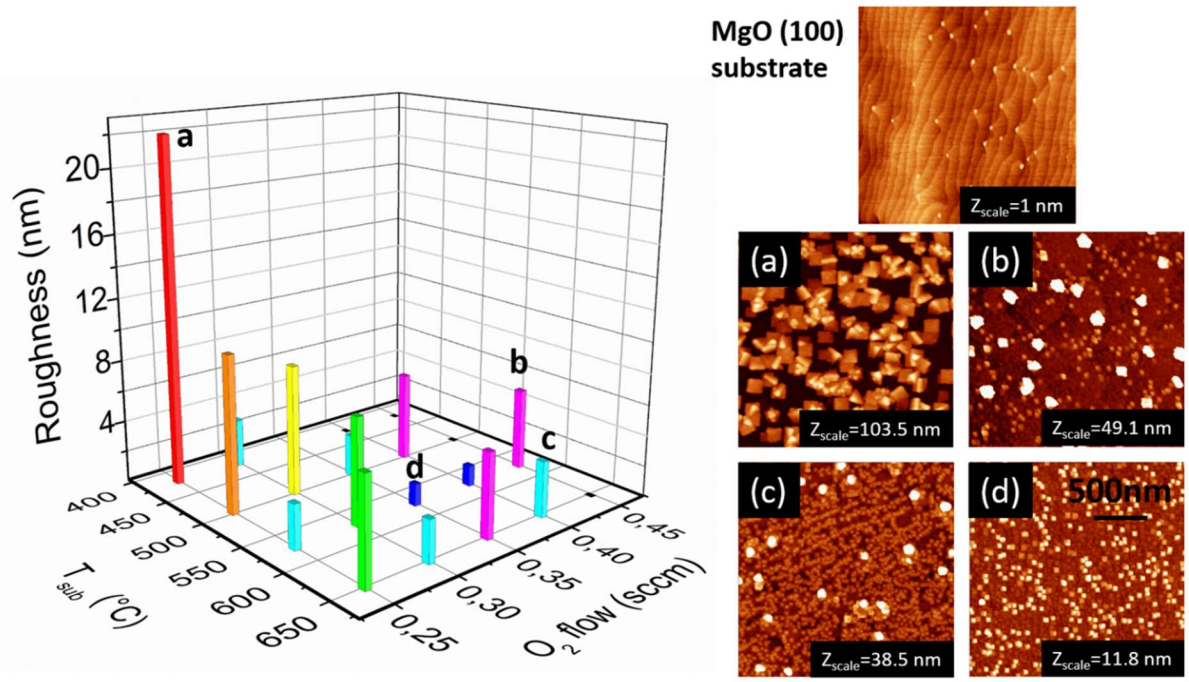
MgO (100)
substrate
Z_scale=1 nm
Roughness (nm)
20
16
12
8
4
a
b
c
d
400
450
500
550
600
650
T_sub (°C)
0,25
0,30
0,35
0,40
0,45
O2 flow (sccm)
(a)
Z_scale=103.5 nm
(b)
Z_scale=49.1 nm
(c)
Z_scale=38.5 nm
(d)
500nm
Z_scale=11.8 nm

Figure 2

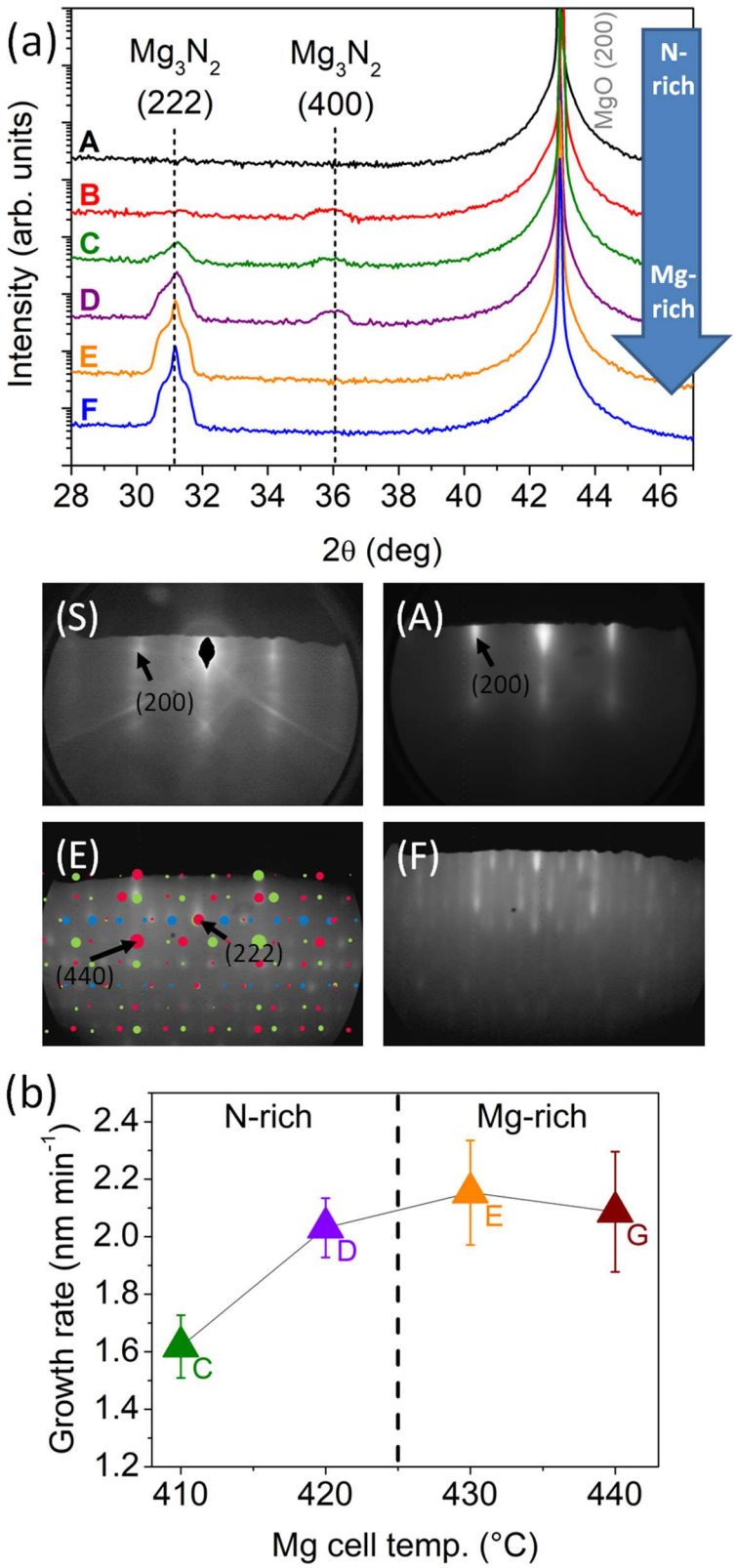
(a)
Mg3N2 (222)
Mg3N2 (400)
MgO (200)
N-rich
Mg-rich
A
B
C
D
E
F
Intensity (arb. units)
28 30 32 34 36 38 40 42 44 46
2θ (deg)
(S)
(200)
(A)
(200)
(E)
(440)
(222)
(F)
(b)
N-rich
Mg-rich
Growth rate (nm min-1)
2.4 2.2 2.0 1.8 1.6 1.4 1.2
C
D
E
G
410 420 430 440
Mg cell temp. (°C)

Figure 3

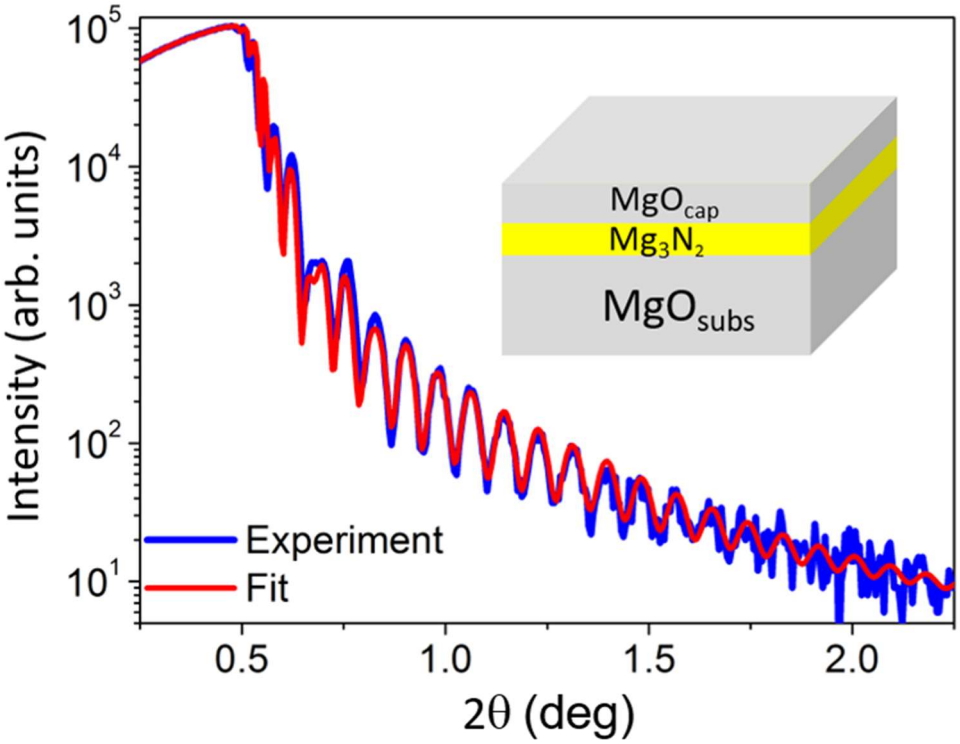
Intensity (arb. units)
10^5
10^4
10^3
10^2
10^1
0.5
1.0
1.5
2.0
2θ (deg)
Experiment
Fit
MgO_{cap}
Mg_3N_2
MgO_{subs}

Figure 4

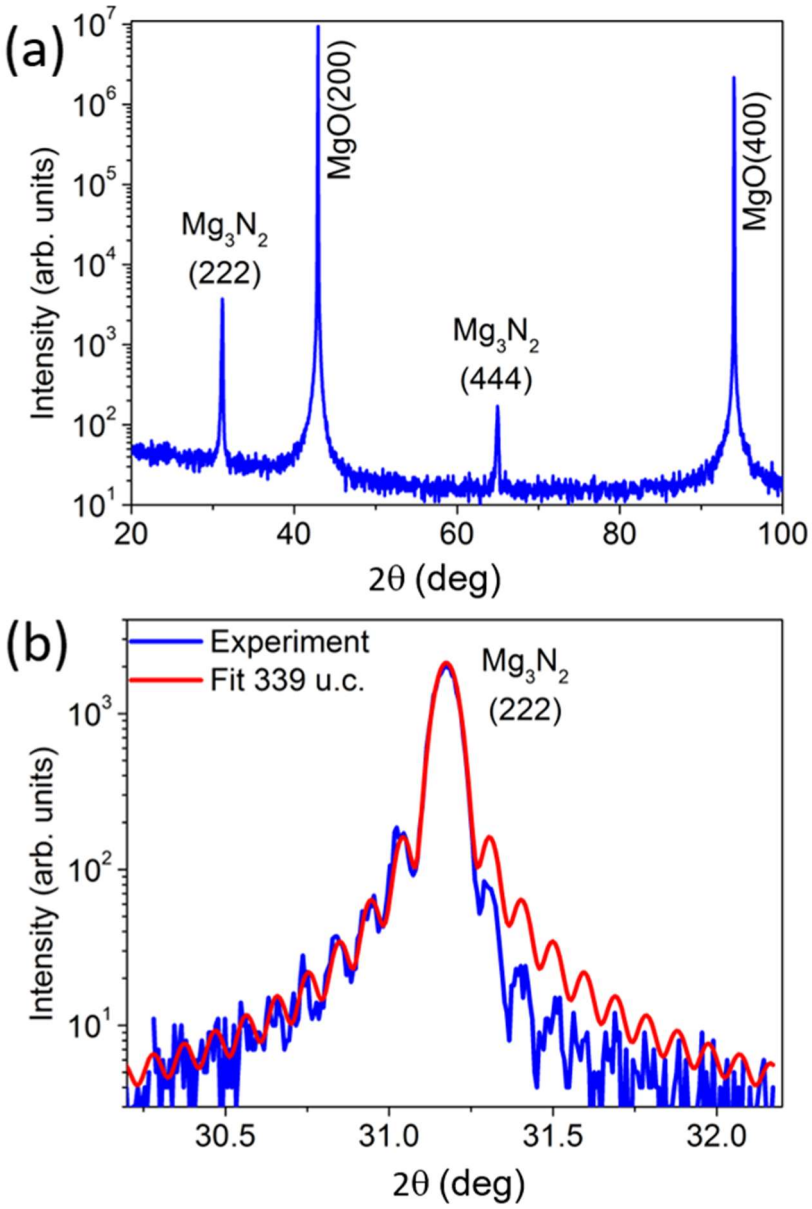
(a)
Intensity (arb. units)
10^7
10^6
10^5
10^4
10^3
10^2
10^1
Mg_3N_2
(222)
MgO(200)
Mg_3N_2
(444)
MgO(400)
20
40
60
80
100
2θ (deg)
(b)
Experiment
Fit 339 u.c.
Mg_3N_2
(222)
Intensity (arb. units)
10^3
10^2
10^1
30.5
31.0
31.5
32.0
2θ (deg)

Figure 5

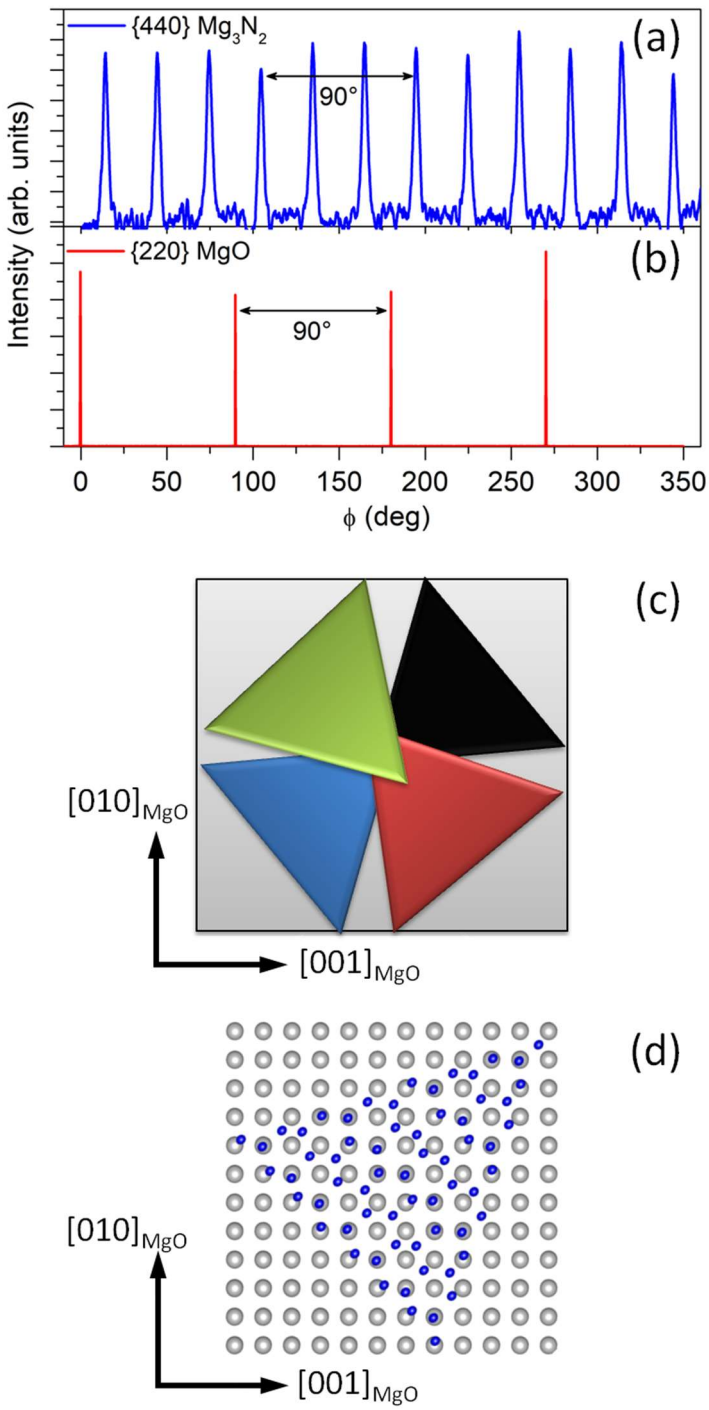
{440} Mg_3N_2
(a)
90°
Intensity (arb. units)
{220} MgO
(b)
90°
0
50
100
150
200
250
300
350
ϕ (deg)
(c)
$[010]_{MgO}$
$[001]_{MgO}$
(d)
$[010]_{MgO}$
$[001]_{MgO}$

Figure 6

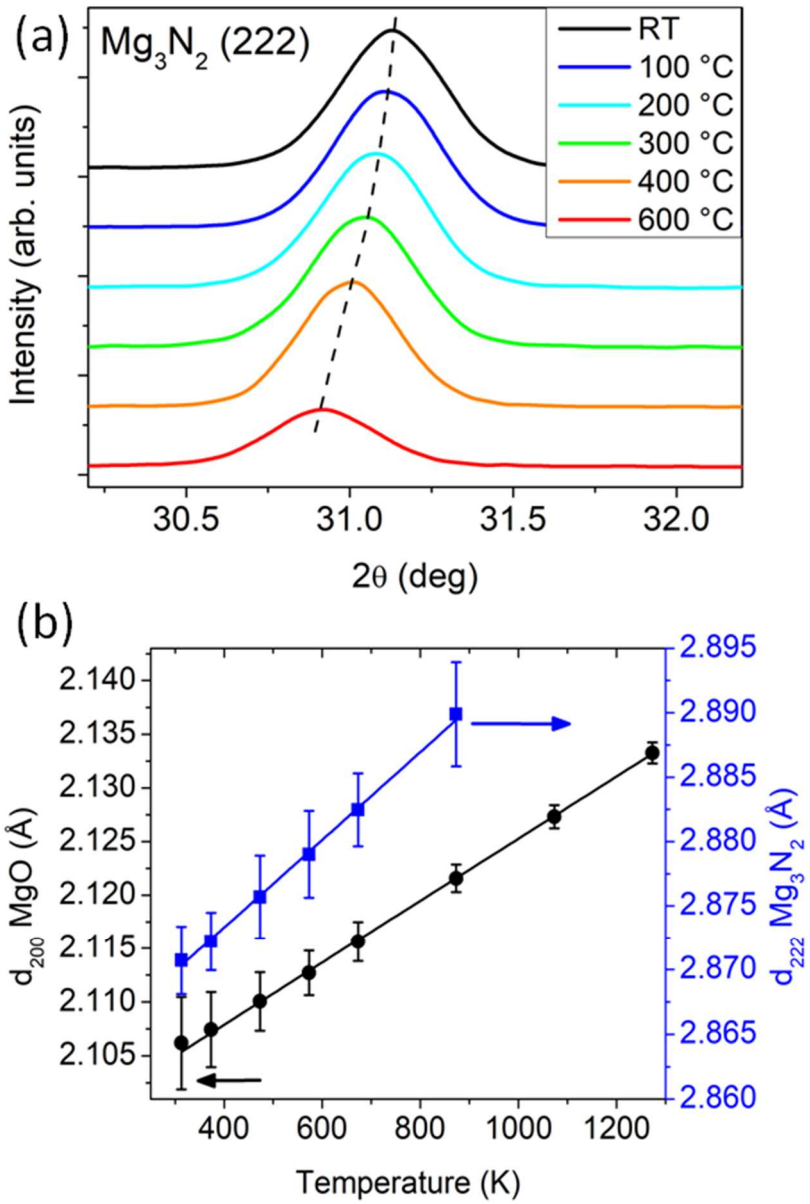
(a)
Mg3N2 (222)
RT
100 °C
200 °C
300 °C
400 °C
600 °C
Intensity (arb. units)
30.5
31.0
31.5
32.0
2θ (deg)
(b)
2.140
2.135
2.130
2.125
2.120
2.115
2.110
2.105
d200 MgO (Å)
2.895
2.890
2.885
2.880
2.875
2.870
2.865
2.860
d222 Mg3N2 (Å)
400
600
800
1000
1200
Temperature (K)

Figure 7

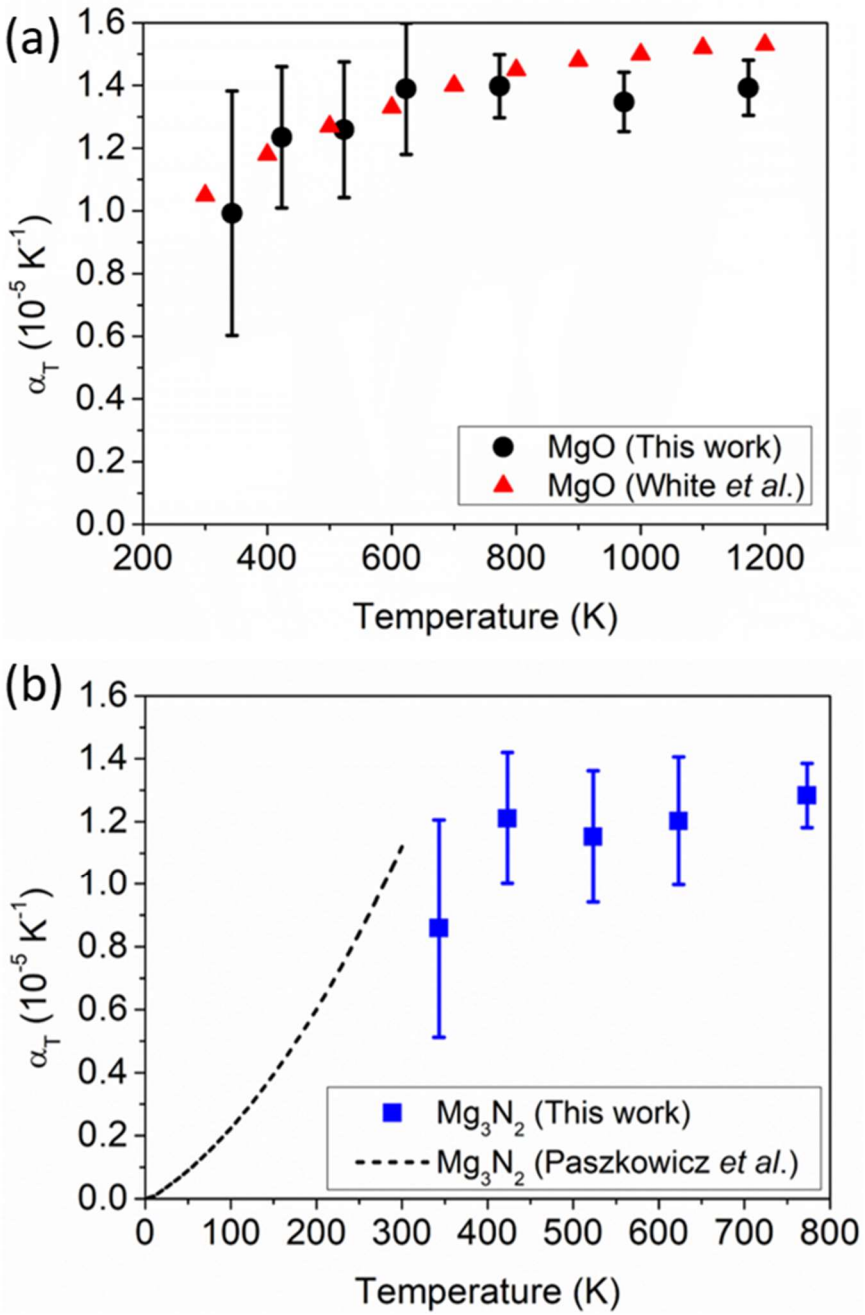
(a)
1.6
1.4
1.2
1.0
0.8
0.6
0.4
0.2
0.0
α_T (10^{-5} K^{-1})
200
400
600
800
1000
1200
Temperature (K)
MgO (This work)
MgO (White *et al.*)
(b)
1.6
1.4
1.2
1.0
0.8
0.6
0.4
0.2
0.0
α_T (10^{-5} K^{-1})
0
100
200
300
400
500
600
700
800
Temperature (K)
Mg_3N_2 (This work)
Mg_3N_2 (Paszkowicz *et al.*)

Figure 8

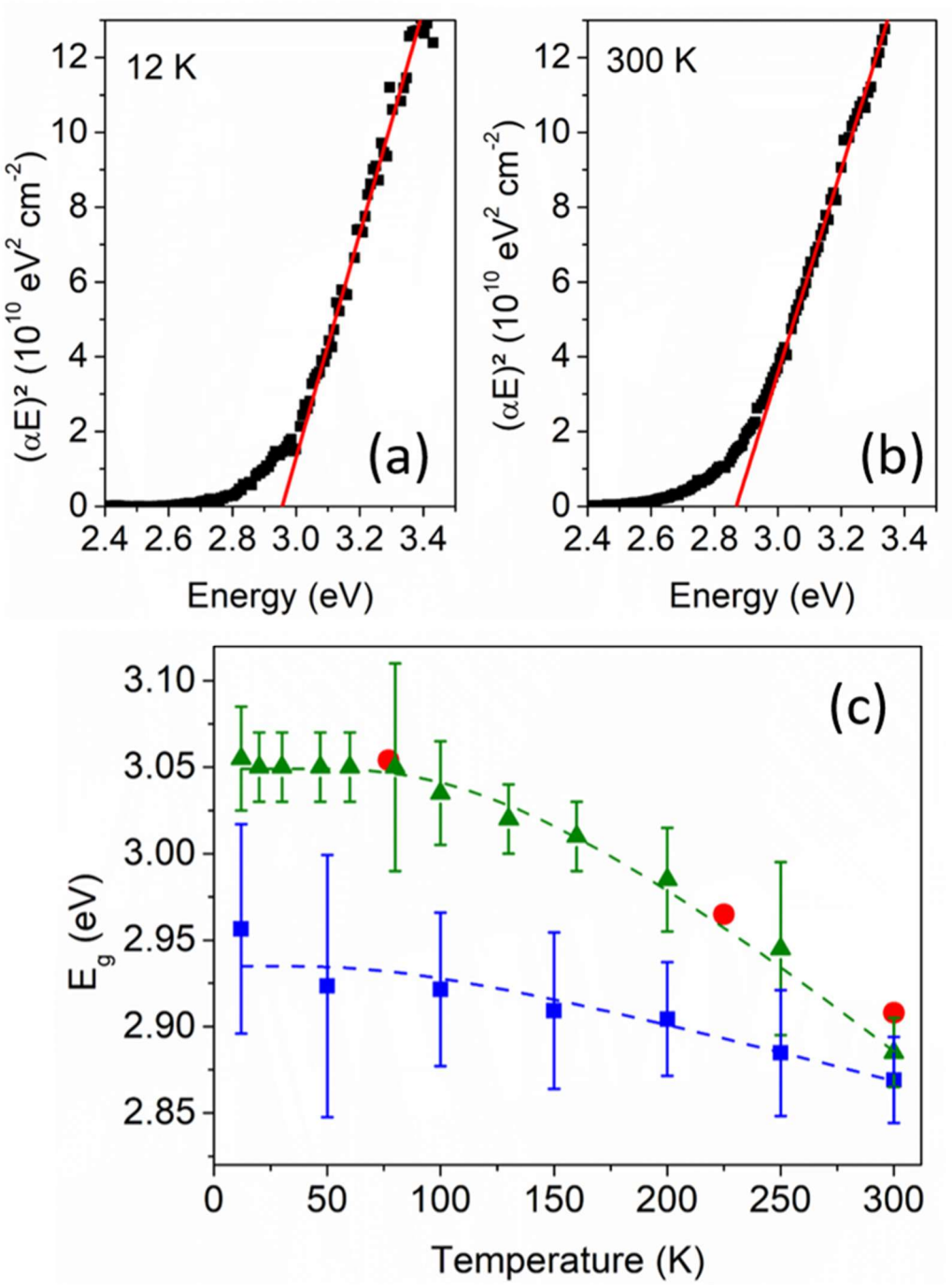
12 K
(a)
(αE)² (10¹⁰ eV² cm⁻²)
Energy (eV)
300 K
(b)
(αE)² (10¹⁰ eV² cm⁻²)
Energy (eV)
(c)
E_g (eV)
Temperature (K)

Figure 9

References

[1] « Bandedge and optical functions of InN", M. Leroux and B. Gil, chapter A4.1 in "Gallium Nitride and Related Semiconductors", Datareviews series, **No. 23** (1998).
[2] V. Yu. Davidov, A. A. Klochikhin, R. P. Seisyan, V. V. Emtsev, S. V. Ivanov, F. Bechstedt, J. Furthmüller, H. Harima, A. V. Mudryi, J. Aderhold, O. Semchinova, and J. Graul, Phys. Status Solidi B **229**, R1 (2002).
[3] V. Yu. Davidov, A. A. Klochikhin, V. V. Emtsev, S. V. Ivanov, V. V. Vekshin, F. Bechstedt, J. Furthmüller, H. Harima, A. V. Mudryi, A. Hashimoto, A. Yamamoto, J. Aderhold, J. Graul and E. E. Haller, Phys. Status Solidi B **230**, R4 (2002).)
[4] M. v. Stackelberg und R. Paulus, Z. Phys. Chem. B **22**, 30 (1933)
[5] D. E. Partin, D. J. Williams, and M. O'Keeffe, J. Sol. Stat. Chem. **132**, 56 (1997)
[6] I. Parkin and A. Nartowski, Polyhedron **17**, 2617 (1998)
[7] H. Ye, X. Liu, and B. Luan, Mater. Lett. **58**, 2361 (2004).
[8] G. Bocquillon, C. Loriers-Susse, and J. Loriers, J. Mater. Sci. **28**, 3547 (1993).
[9] Z. Lences, K. Hirao, Y. Yamauchi, and S. Kanzaki, J. Am. Ceram. Soc. **86**, 1088 (2003)
[10] U. Ash-Kurlander, G. E. Shter, S. Kababya, A. Schmidt, and G. S. Grader, J. Phys. Chem. C **117**, 1237 (2013).
[11] C. M. fang, R. A. de Groot, R. J. Bruls, H. T. Hintzen, and G. de With, J. Phys.: Cond. Mat. **11**, 4833 (1999).
[12] E. Orhan, S. Jobic, R. Brec, R. Marchand, and J. Y. Saillard, J. Mater. Chem. **12**, 2475 (2002).
[13] M. G. Moreno Armenta, A. Reyes-Serrano, and M. Avalos Borja, Phys. Rev. B **62**, 4890 (2000).
[14] P. Wu and T. Tiedje, Appl. Phys. Lett. **113**, 082101 (2018).
[15] Y. Uenaka and T. Uchino, J. Phys. Chem. C **118**, 11895 (2014).
[16] K. Toyoura, T. Goto, K. Hachiya, and R. Hagiwara, Electrochem. Acta **51**, 56 (2005).
[17] P. Wu, X. Cao, T. Tiedje and N. Yamada, Mater. Lett. **236**, 649 (2019).
[18] P. Vennéguès, M. Benaissa, B. Beaumont, E. Feltin, P. de Mierry, S. Dalmasso, M. Leroux, and P. Gibart, Appl. Phys. Lett. **77**, 880 (2000).
[19] M. Hansen, L. F. Chen, S. H. Lim, S. P. DenBaars, and J. S. Speck, Appl. Phys. Lett. **80**, 2469 (2002).
[20] P. Vennéguès, M. Leroux, S. Dalmasso, M. Benaissa, P. De Mierry, P. Lorenzini, B. Damilano, B. Beaumont, J. Massies, and P. Gibart, Phys. Rev. B **68**, 235214 (2003).
[21] D. R. Glasson and S. A. A. Jayaweera, J. Appl. Chem. **18**, 77 (1968).
[22] X. D. Peng, D. S. Edwards, and M. A. Barteau, Surf. Sci. **195**, 103 (1988).
[23] A. M. Heyns, L. C. Prinsloo, K. J. Range, and M. Stassen, J. Sol. Stat. Chem. **137**, 33 (1998)
[24] K. J. Chang and M. L. Cohen, Phys. Rev. B **30**, 4774 (1984).
[25] M. Björck and G. Anderson, J. Appl. Cryst. **40**, 1174 (2007).
[26] J. Triscone, P. Fivat, M. Andersson, M. Decroux, and O. Fischer, Phys. Rev. B **50**, 1229 (1994).
[27] J. Bläsing, A. Krost, J. Hertkorn, F. Scholz, L. Kirste, A. Chuvilin, and U. Kaiser, J. Appl. Phys. **105**, 033504 (2009).
[28] M. Grundmann, T. Böntgen, and M. Lorenz, Phys. Rev. Lett. **105**, 146102 (2010).
[29] M. Grundmann, Phys. Stat. Sol. B **248**, 805 (2011).
[30] P. Lautenschlager, P. B. Allen, and M. Cardona, Phys. Rev. B **31**, 2163 (1985).
[31] G. A. Slack, and S. F. Bertram, J. Appl. Phys. **46**, 89 (1975).
[32] F. Liu and B. Zheng, Powder Diffr. **6**, 147 (1991).
[33] F. Liu, Powder Diffr. **8**, 36 (1993).
[34] R. J. Beals, and R. L. Cook, J. Am. Ceram. Soc. **40**, 279 (1957).
[35] G. K. White and O. L. Anderson, J. Appl. Phys. **37**, 430 (1966).
[36] W. Paszkowicz, M. Knapp, J. Z. Domagala, G. Kamler, and S. Podsiadlo, *J. All. Comp.* **328**, 2372 (2001)
[37] H. Ibach, phys. stat. sol. 31, 625 (1969)
[38] H. Ibach, phys. stat. sol. 33, 257 (1969)

[39] H. Köncke, S. Figge, B. M. Epelbaum, and D. Hommel, Act. Phys. Pol. A **114**, 1193 (2008)
[40] F. Datchi, A. Dewaele, Y. Le Godec, and P. Loubeyre, Phys. Rev. B **75**, 214104 (2007).
[41] M. Leszczynski, T. Suski, H. Teyssiere, P. Perlin, I. Grzegory, J. Jun, S. Porowski, and T. D. Moustakas, J. Appl. Phys. **76**, 4909 (1994).
[42] Y. Varhsni, Physica **34**, 149 (1967)
[43] K. P. O'Donnell and X. Chen, Appl. Phys. Lett. **58**, 2924 (1991)
[44] I. Vurgaftman, J. R. Meyer, and L. R. Ram-Mohan, J. Appl. Phys. **89**, 5815 (2001).
[45] S. Biernacki, U. Scherz, and B. K. Meyer, Phys. Rev. B **49**, 4501 (1994).
[46] R. Dagher, L. Lymperakis, V. Delaye, L. Largeau, A. Michon, J. Brault, and P. Vennéguès, Sci. Rep. 9, 15907 (2019)
[47] F. Semond, E. Frayssinet and J. Massies, US2018/0012753